Chemical Process Design Vol.2 No.1 (2023) 32-42

University of Sistan and Baluchestan

Chemical Process Design

Available online at http://cpd.usb.ac.ir/



Computational Modeling of Toluene Removal in a Photocatalytic Membrane-based Reactor

Morteza Golmohammadi[1*], Fatemeh Ziaei Moghaddam[2]

[1] Department of Chemical Engineering, Birjand University of Technology, Birjand, Iran
[2] Chemical Engineering Department, Faculty of Engineering, Ferdowsi University of Mashhad, Mashhad, Iran

ARTICLE INFO

Article history:
Received: 2022-09-19
Received in revised form: 2023-08-09
Accepted: 2023-08-10
Published online: 2023-08-10

Keywords:
Membrane reactor; Modeling; Volatile organic carbon; Photocatalyst

DOI: *10.22111/CPD.2023.43496.1007*

ABSTRACT

Volatile Organic Compounds (VOCs) are a large group of chemicals that are found in many products. The VOCs emission has become a serious challenge due to their adverse effects on human health and the ecological environment. Consequently, the development of various technologies to eliminate VOCs is an undeniable necessity. To develop an effective elimination technique, computational modeling is a powerful tool for process assessment. In this study, computational modeling was conducted to analyze the transport phenomena during the photocatalytic degradation of toluene, in a supported ionic liquid membrane reactor. The mass transfer coefficient and reaction rate constant were estimated and the flux magnitude and flux streamlines were also determined and analyzed. Furthermore, the membrane permeance was also determined as a function of membrane channel length and time. The accuracy of the model was confirmed by fitting the actual average concentration of the toluene and the values predicted by the model over time.

1. Introduction

Volatile organic compounds (VOCs) are carbon-containing compounds with high vapor pressure that simply evaporate and are released as gases from certain solids or liquids [1]. These compounds are usually emitted from outdoor sources, e.g. energy production industries, manufacturing industries, transportation, small-scale combustion, industrial processes, solvents, agriculture, landfills, and indoor sources, e.g. all materials made of organic compounds such as printers, carpets cars, paints, adhesives, cigarette smoke, etc. [2, 3]. VOCs are harmful to the atmosphere, human health and the ecological environment [4]. Most VOCs such as aldehydes, aromatic compounds, polycyclic aromatic hydrocarbons, alcohols and ketones, etc., are highly toxic and carcinogenic [1]. Moreover, VOCs play an important role in the formation of ozone and secondary organic aerosols in the ambient air and are considered the main cause of smog, which has harmful effects on human health [5, 6]. Hence, it is of great importance and urgency

Corresponding author. Tel.: +98 56 32391229; Fax: +98 53 32391238
E-mail address: Golmohammadi@birjandut.ac.ir (M. Golmohammadi)

to develop effective VOC abatement techniques. There are various techniques to control the release of VOC, including recovery methods such as adsorption [7], condensation [8], absorption [9], and membrane separation [10] and destruction methods such as ozone catalytic oxidation [11], photocatalytic oxidation [12], plasma catalysis [13], and biodegradation [14]. Among these methods, photocatalytic oxidation devoted considerable attention because of its energy-saving advantage, excellent performance and process simplicity [15-17]. A great deal of research has been conducted to examine the performance of various photocatalytic systems, including photocatalytic membrane-based reactors as a combination of photocatalysis with membrane separation [18-20]. Since the supported liquid exhibits higher VOC permeability and selectivity, compared to conventional polymer membranes, they have recently received more attention [21]. Ionic liquids are suitable liquid for supported liquid membranes due to their unique properties such as low flammability, low volatility and high thermal stability [22-24].

The design and construction of catalytic reactors require an understanding of reaction kinetics, mass and heat transfer rates, and hydrodynamics [25]. Hence, a more profound insight into the physical and chemical phenomena occurring in catalytic reactors is very important for the design of catalytic processes. Computational modeling and simulation is a very useful tool for the design, development, analysis, optimization, and scale-up of various types of catalytic membrane reactors [26, 27]. Phan et al. [28] developed a quantitative model to investigate the influence of mass transfer rate and intrinsic reaction rate on the overall photocatalytic degradation of methylene blue in a fixed-bed photocatalytic membrane reactor. Their results showed that the mass transfer rate contributes considerably to the overall reaction rate constant. Zak et al. [29] constructed a computational model to investigate the impact of various parameters on the performance of the catalytic hydrogel membrane reactor. According to their modeling, it was found that mass transfer becomes limiting as the catalytic hydrogel thickness increases.

This work is focused on the computational modeling of toluene photocatalytic degradation under UV irradiation using a supported ionic liquid membrane reactor based on experimental results achieved by Li et al. [21]. Their work was mainly devoted to the synthesis and characterization of the membrane, as well as evaluation of its performance in the removal of some VOCs. The objective of the current study was to present a detailed analysis of the transport phenomena and to estimate important transport coefficients such as the mass transfer coefficients and the rate of reaction coefficient. The magnitude and streamlines of mass flux were determined and analyzed. The membrane permeance was also assessed as a function of membrane channel length and time. The model was verified by fitting the results on the experimental data and could correctly predict the behavior of the system.

2. Materials and methods

The details of the experimental setup and experiment procedures are published in a previous work [21]. Briefly, the test chamber is a cube with a volume of 0.5m^3, in which toluene is mixed with air at a homogeneous concentration of 1000ppm. The membrane reactor is placed in the center of the test chamber, which has a surface area of 0.065 m^2. Air with a flow rate of 0.5 L/min is passed through the permeate channel, which is maintained at a vacuum level of 10kPa throughout the experiment. The air flow is from left to right and the membrane flux is normal to its surface. The geometry of the system is shown in Fig. 1. Because of the symmetry of the system, a two-dimensional (2D) model was considered to reduce the computational cost.

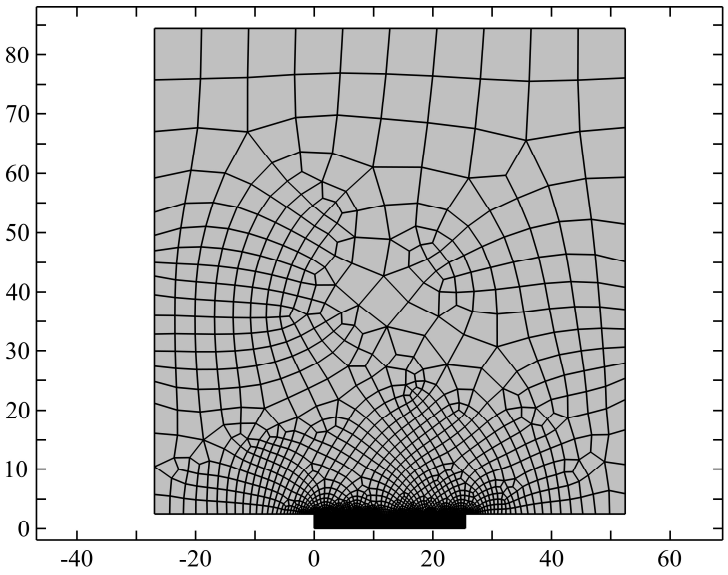


Fig. 1. Model geometry and mesh

3. Model development

The assumptions made in this modeling are:

- Because of low concentration of toluene (1000ppm), the heat of reaction can be neglected, and the system assumes isothermal.
- The membrane is coated homogenously, so isotropic reaction rate coefficient is considered.
- Laminar compressible flow due to the low velocity of air (2×10^{-5} m/s)
- Lumped capacitance for membrane and support
- The gas mixture considers ideal gas law, because of low concentration of toluene and low pressure of system ($\leq$ 1atm)
- No slip condition at surfaces

The famous Navier-Stokes equation is solved to obtain the velocity and pressure fields in the geometry [30].

$$\rho\frac{\partial u}{\partial t}+\rho(u.\nabla)u=\nabla.\left[-pI+\boldsymbol{K}\right]+\rho g \tag{1}$$

$$\boldsymbol{K}=\left(\mu+\mu_T\right)\left(\nabla u+(\nabla u)^T\right) \tag{2}$$

$$\rho\nabla.u=0 \tag{3}$$

where u is velocity, t is time, , ρ is density, p is pressure, μ is dynamic viscosity, and μ_T is the turbulent dynamic viscosity. Moreover, the mass transfer equation reads:

$$\frac{\partial C_i}{\partial t}+\nabla.J_i+u.\nabla C_i=R_i \tag{4}$$

$$J_i=-D_i\nabla C_i \tag{5}$$

where C_i is the toluene concentration, u is the velocity vector, R_i is the reaction term, and D_i is the effective diffusivity coefficient. The initial concentration of toluene in the test chamber is 1000 ppm and the permeate channel is free of toluene. There is no flow in the system at the beginning of the experiment. The test chamber is at atmospheric pressure and the pressure in the permeate channel is 10kPa absolute. Therefore, the initial conditions read:

$$u_{cham.}=0\ ,\ p_{cham.}=101.3kPa,\ p_{chan.}=10kPa,\ C_{i,cham.}=1000\,ppm,\ C_{i,chan.}=0$$

where the subscripts *cham.* and *chan.* refer to test chamber and permeate channel, respectively.

Two boundary conditions are critical for accurate modeling results. First one is the flux at the membrane surface; and second is the fresh air input valve for preventing negative pressure in the chamber. Standard no flux boundary condition ($n.J_i = 0$) was used for other surfaces. According to the experimental results, toluene molecules permeate through the membrane and the nanoparticle coating on the surface of the membrane. UV irradiation degrades the majority of toluene, but some toluene molecules, are carried away from the membrane surface by the air flow in the permeate channel. According to the reaction mechanisms and the experimental results discussed in the previously published work [21], the reaction follows a pseudo first order kinetics. Therefore, the flux through the membrane has two terms and can take the following form:

$$n.J_i = k_o(C_{i,u} - C_{i,d}) - k_r C_{i,u} \tag{6}$$

where n is the normal vector of the boundary, J_i is the flux at the boundary, $k_o$is the overall mass transfer coefficient, $C_{i,u}$is the toluene concentration upside the boundary, $C_{i,d}$ is the toluene concentration downside the boundary conditions, and $k_r$is the reaction rate constant. According to the lumped capacitance assumption, the overall mass transfer resistance ($1/k_o$) is the sum of laminar film resistance in the feed side, resistance of the nanoparticle coating, resistance of the membrane, resistance of the support, and the laminar film resistance in the permeate side. The following Sherwood correlation is commonly used to estimate the overall mass transfer coefficient [31]:

$$Sh = \frac{k_o d_h}{D} = 1.62(\mathrm{Re}\,Scd_h/L)^{0.33} \tag{7}$$

where Sh is the Sherwood number, k_o is the overall mass transfer coefficient, Re is the Reynolds number, Sc is the Schmidt number, d_h is the hydraulic diameter of the membrane, and L is the membrane channel length. k_r is determined by fitting the model results on the experimental data.

The second boundary condition is the fresh air input, which is defined as an open boundary condition. This boundary condition takes the following form:

$$\begin{aligned} -n.J_i &= 0 \quad if\ n.u \geq 0.8 \\ C_i &= 0 \quad if\ n.u < 0 \end{aligned} \tag{8}$$

The system of equations is solved using COMSOL Multiphysics solvers. The computer system specs used for the computations were 8 CPU cores (i9-9900K, 4.2 GHz) and 32GB of processing memory.

4. Results and discussion

The velocity and relative pressure profiles determined from the Navier-Stokes equation are shown in Fig. 2(a) and (b). The laminar flow profile of the sweep gas in the permeate channel can be seen. The test chamber is initially filed with a mixture of air and toluene with a toluene concentration of 1000ppm. During the experiment, the test chamber is at atmospheric pressure (relative pressure is zero) while the permeate channel is kept at 10kPa using a vacuum pump (relative pressure is 10kPa). This transmembrane pressure gradient is a driving force for the toluene permeation. Noteworthy is that the maximum velocity occurred at the center of the channel, while it was zero at the surface of the channel.

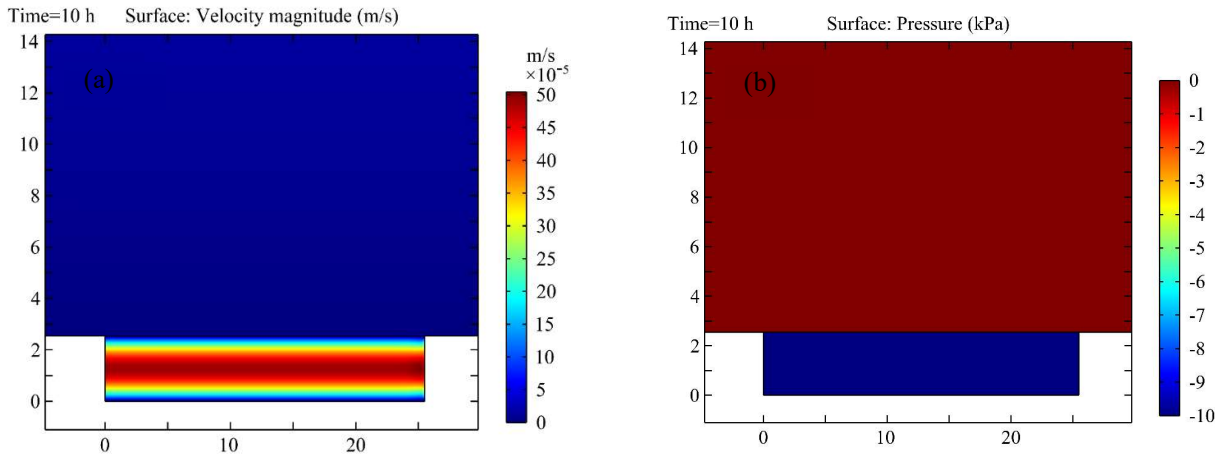


Fig. 2. (a) Velocity profile, and (b) Pressure profile of the system

The concentration of toluene in the test chamber is analyzed over time. It can be seen in Fig. 3(a) that the concentration of toluene near the membrane decreased at t = 15 minutes because of the surface flux at the membrane, which is as a result of both the photocatalytic reaction and the permeation to the other side of the membrane. To avoid negative pressure in the chamber, very low amounts of fresh air are injected into the chamber through an inlet settled at the left wall of the chamber. Accordingly, as can be seen in Fig. 3 the concentration of toluene is low in the vicinity of the inlet. The black lines in this figure show the flux streamlines in the test chamber. These lines clearly illustrate the transport phenomenon and help better understand it. At t = 15 minutes, the majority of flux is at the lower zone of the test chamber where a concentration gradient exists. At t = 1 hour, the concentration of toluene in the chamber near the membrane zone further decreases as a result of simultaneous mass transfer and reaction over time (Fig. 3(b)). The concentration of toluene in the chamber decreases over time and the concentration profile at t = 3 and 10 hours are shown in Fig. 3(c) and (d), respectively.

As seen, the mass transfer zone has reached the upper zones of the test chamber. Some flux streamlines show the transport of toluene from the top of the test chamber towards the membrane, which was not seen at t = 15 minutes and t = 1 hour. This observation is a result of the mass transfer propagation due to concentration gradient in the test chamber over time.

The flux magnitude and streamlines in the permeate side of the membrane are demonstrated in Fig. 4(a) and Fig. 4(b). The sweep gas, which is entering the channel from the left side, carries away the permeated Toluene. The magnitude of the flux is higher at the center line of the channel due to the velocity profile of the laminar flow as seen in Fig. 2(a). The magnitude of flux in the sweep gas is decreased over time as can be seen in Fig. 4(b).

According to the color legends in Fig. 4(a) and (b), the maximum flux at the center line of the permeate channel decreased from 18×10^{-4}mol/m^2.s to 20×10^{-5}mol/m^2.s. This observation is attributed to the higher concentration gradient across the membrane at the beginning of the experiment and the decrease in test chamber concentration with time.

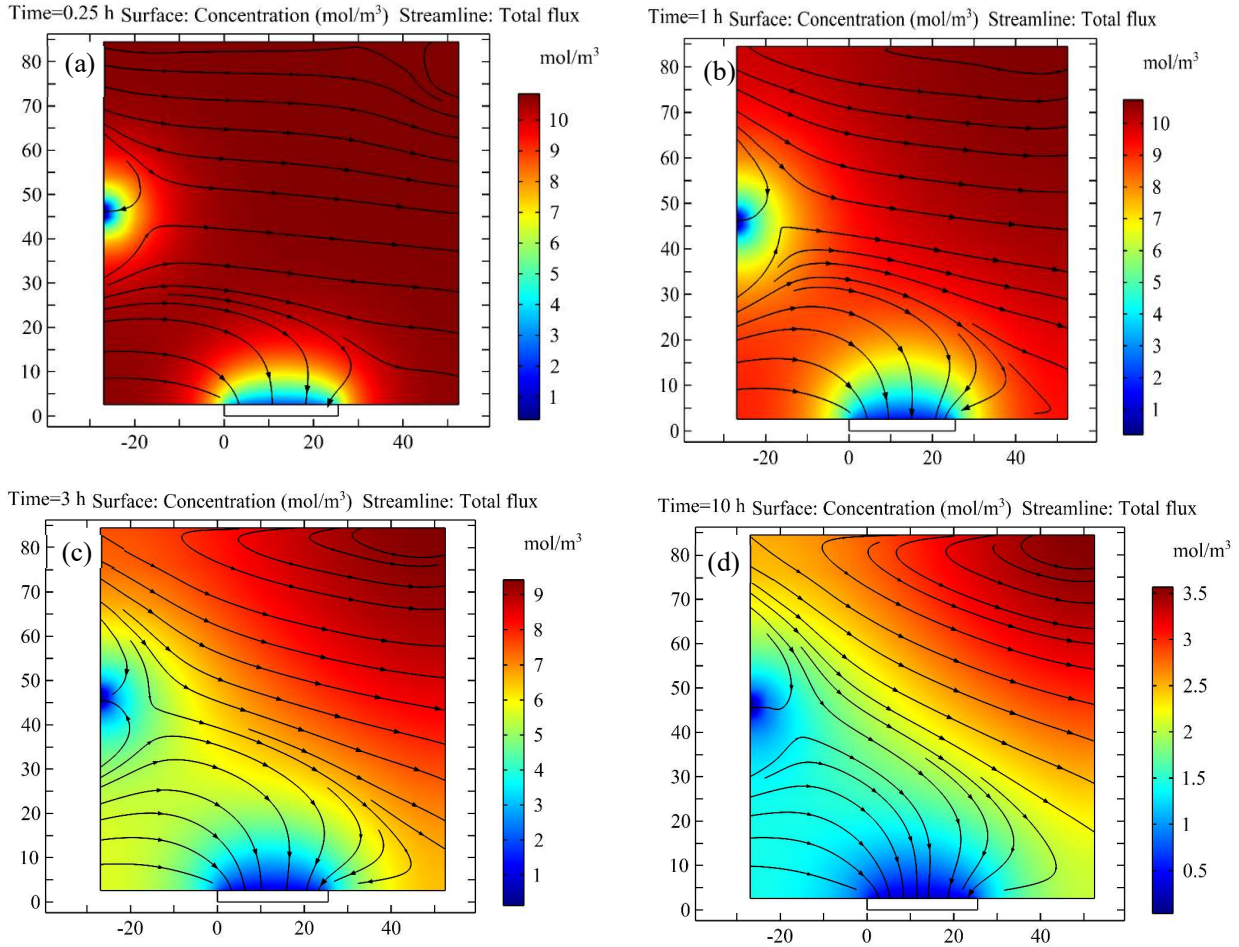


Fig. 3. Concentration profile of toluene in the chamber at: (a) t = 0.25h, (b) t = 1h, (c) t = 3h, and (d) t = 10h

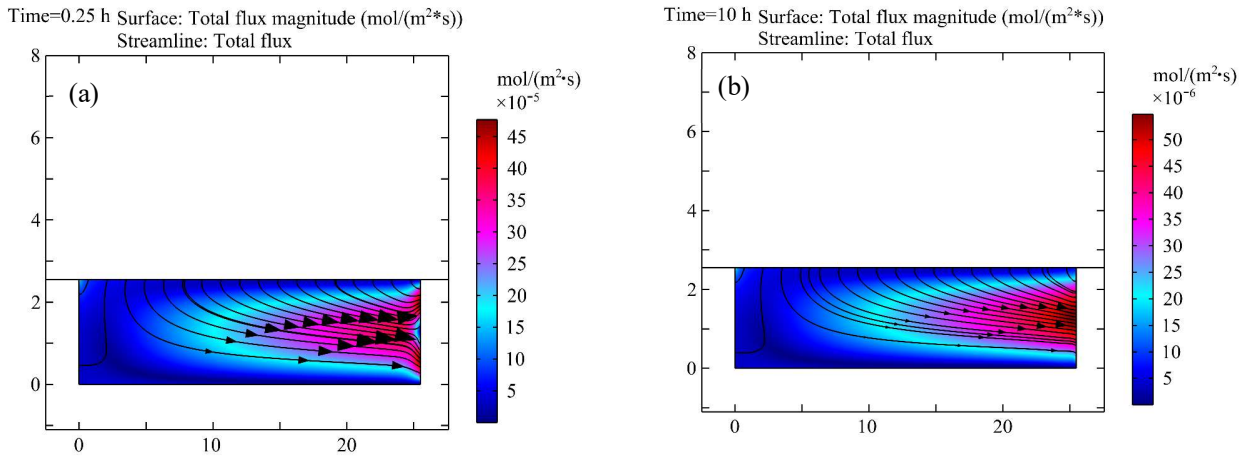


Fig. 4. Toluene flux profile in the permeate channel at: t = 0.25h, and (b) at t = 10h

Fig. 5 shows the average concentration of toluene at the outlet of the permeate channel. It is obvious that the concentration increases first and reaches its maximum value after approximately 0.5 hours and then decreases. The average concentration increase in the first half hour was due to the UV lamp being off during this time to the adsorption-desorption equilibrium of gaseous toluene on the surface of the membrane was achieved. After this time,

when the UV lamp was turned on and consequently the photocatalytic reaction started, the average concentration of toluene at the outlet of the permeate channel gradually decreased. Moreover, as mentioned before, toluene permeates through the membrane while the photocatalytic reaction is taking place on the surface of the membrane. Hence, this decrease is the result of both reaction and the decreasing concentration of toluene in the feed chamber.

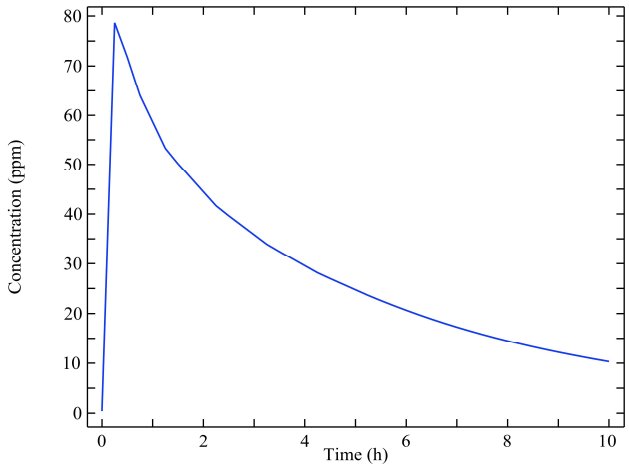


Fig. 5. Average toluene concentration in the permeate channel outlet over time

Fig. 6 shows the normal flux at the membrane surface across its length. The decreasing flux can be seen over time due to decrease of chamber test concentration. The flux around the membrane corners is higher because of the concentration profile at the zone above the membrane (see Fig. 3). Because the test chamber has a larger cross sectional surface area than the membrane, the flux streamlines and concentration gradient around the corners are different from those in the middle section of the membrane.

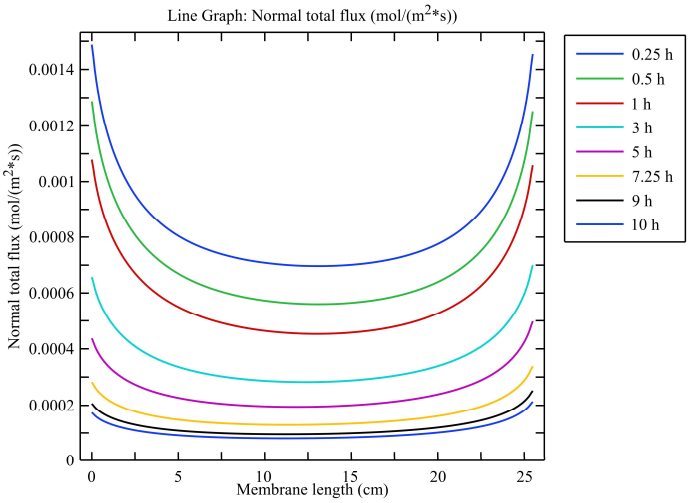


Fig. 6. Normal toluene flux as a function of membrane length at different times throughout the experiment

Fig. 7 shows the average permeance for ten hours. Similarly, membrane permeance decreases over time as the concentration gradient reduces. The sharp decrease relates to the first half hour before the UV lamp turned on and the reaction started. As seen in Fig. 5, during this time, the concentration in the permeate channel increases quickly;

therefore, the gradient concentration and permeance of the membrane fall. The flux magnitude and streamlines in both domains are shown in Fig. 8 for better visualization and understanding of the transport phenomena. The reaction rate on the surface of the membrane is plotted over time in Fig. 9. It can be seen that the rate decreases over time because of the decreasing concentration in the feed chamber and at the top of the membrane surface.

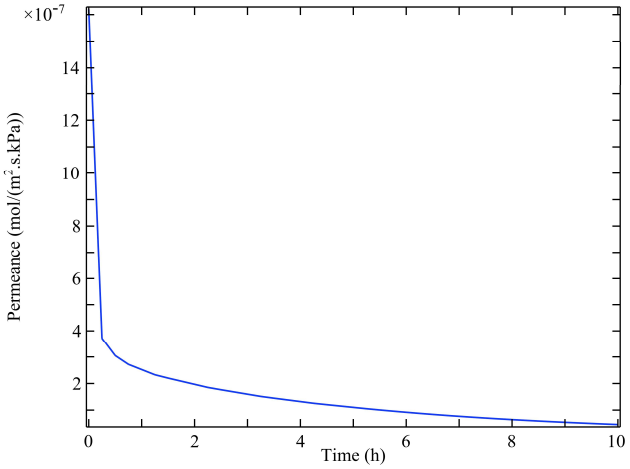


Fig. 7. Membrane permeance over time

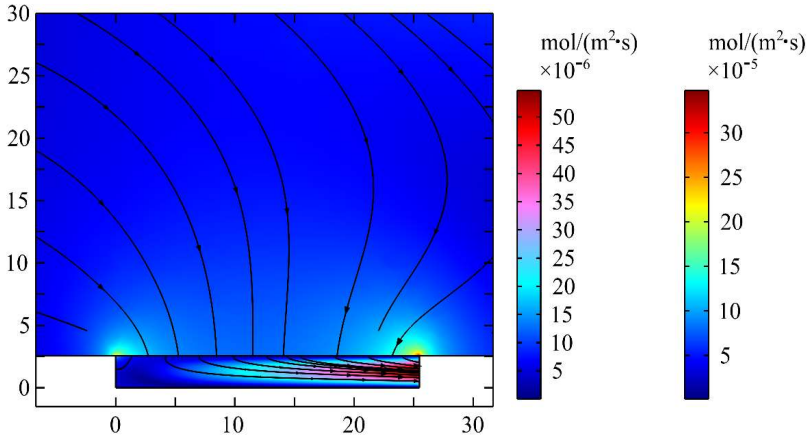


Fig. 8. Flux magnitude and streamlines in both domains

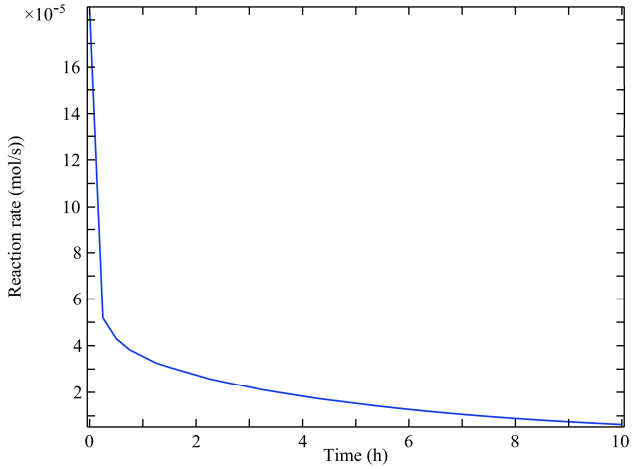


Fig. 9. The surface reaction rate over time

The modeling results were fitted on the experimental data to verify the model. The average concentration of the toluene in the chamber is plotted over time and compared to the values determined experimentally by GC (experimental data from reference [21]). As can be seen in Fig. 10, the model correctly predicts the behavior of the system (R^2 = 0.988). A value of 2.9×10^{-4} m/s was determined for the reaction rate constant (k_r). According to this analytical equation, the reaction coefficient is $(V/At)Ln(C_0/C_t)$ where V is the volume of the chamber, A is the cross-sectional area of the membrane, t is the time, C_0 is the initial concentration, and C_t is concentration at reaction time t. The overall mass transfer coefficient (k_o) was 1.49×10^{-5}m/s, which was determined using Eq. 7. The effective diffusivity of toluene in air was 0.087cm^2/s [32].

The modeling results slightly deviate from the experimental data at t >7 hours. This observation could be because of the deactivation of nanoparticles as the photocatalyst. In the model, the reaction coefficient is not a function of time, while the activity of the photocatalyst and the reaction rate may decrease over time. Membrane fouling could also be a reason, as it was observed in the experiments that minor amounts of toluene permeate through the membrane without reaction. The adsorption of toluene and air molecules is not likely to be the reason for the observed deviation because the membrane was exposed to the mixture of air - toluene in the dark for a few hours before starting the experiment.

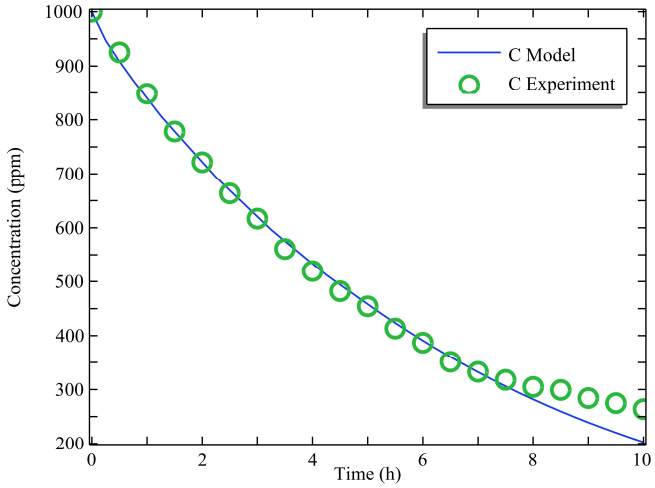


Fig. 10. Model fitting on the experimental data; the model could correctly predict the behavior of the system (experimental data from reference [21])

Conclusion

Photocatalytic degradation of toluene in a membrane reactor was analyzed using computational modeling. The model was verified using experimental data and the mass transfer and reaction rate coefficients were determined. The main aspects of the transport phenomena such as the flux magnitude and flux streamlines, membrane permeance, and fluid dynamics were investigated and visualized as a function of time and geometrical coordinates. The modeling results provide very useful insights and information for research and development of advanced membrane reactors. The pressure gradient caused the permeation of the toluene molecules through the membrane from the feed chamber to the permeate chamber. Meanwhile, most of the permeating toluene degraded via photocatalytic reaction. The permeation and degradation resulted in the decrease of the toluene concentration in the feed chamber and a subsequent decrease in the reaction rate and mass flux over time. Besides, the larger cross-sectional area of the feed chamber

compared with the permeate chamber invoked higher flux around the corner of the membrane. Moreover, the reaction rate constant was determined 2.9×10^{-4}m/s via fitting experimental data with the model. But slight deviation of modeling results from experimental data at t >7 hours indicate the deactivation and fouling of the membrane. This effect can be studied further in future work, considering the reaction rate constant as a function of time.

Acknowledgement

We gratefully acknowledge the support and funding from Birjand University of Technology.

Nomenclature

Symbols

C	Concentration (ppm)
d_h	Hydraulic diameter (m)
D	Molecular diffusivity (m^2/s)
j	Mass flux ($kg/m^2/s$)
k_r	Reaction constant (1/s)
k_o	Overall mass transfer coefficient (m/s)
p	Pressure (N/m^2)
R	Reaction rate (mol/m^3s)
Sh	Sherwood number
Re	Reynolds number
Sc	Schmidt number
t	Time (s)
u	Velocity (m/s)

Greek letters

μ	Dynamic viscosity ($N.s/m^{2)}$
ρ	Density (kg/m^3)

Subscripts

Cham.	Test chamber
Chan.	Permeate channel
d	Downside
i	Component (Toluene)
T	Turbulent
u	Upside

References

[1] Zhang, X., Gao, B., Creamer, A.E., Cao, C., Li, Y., 2017. Adsorption of VOCs onto engineered carbon materials: A review. Journal of hazardous materials, 338, 102-123. https://doi.org/10.1016/j.jhazmat.2017.05.013
[2] Huang, L., Wei, Y., Zhang, L., Ma, Z., Zhao, W., 2021. Estimates of emission strengths of 43 VOCs in wintertime residential indoor environments, Beijing. Science of The Total Environment, 793, 148623. https://doi.org/10.1016/j.scitotenv.2021.148623
[3] Arias, F.J., de las Heras, S., 2017. Use of hydrodynamic cavitation for volatile removal compound. International Journal of Heat and Fluid Flow, 66, 1-7. https://doi.org/10.1016/j.ijheatfluidflow.2017.05.001
[4] Qian, W., Guo, Y., Wang, X., Qiu, X., Ji, X., Wang, L., et al., 2022. Quantification and assessment of chemical footprint of VOCs in polyester fabric production. Journal of Cleaner Production, 339, 130628. https://doi.org/10.1016/j.jclepro.2022.130628
[5] Kansal, A., 2009. Sources and reactivity of NMHCs and VOCs in the atmosphere: A review. Journal of hazardous materials, 166(1), 17-26. https://doi.org/10.1016/j.jhazmat.2008.11.048
[6] Xiong, Y., Zhou, J., Xing, Z., Du, K., 2020. Optimization of a volatile organic compound control strategy in an oil industry center in Canada by evaluating ozone and secondary organic aerosol formation potential. Environmental Research, 191, 110217. https://doi.org/10.1016/j.envres.2020.110217
[7] Tatin, R., Moura, L., Dietrich, N., Baig, S., Hébrard, G., 2015. Physical absorption of volatile organic compounds by spraying emulsion in a spray tower: Experiments and modelling. Chemical Engineering Research and Design, 104, 409-415. https://doi.org/10.1016/j.cherd.2015.08.030
[8] Wang, H., Guo, H., Zhao, Y., Dong, X., Gong, M., 2020. Thermodynamic analysis of a petroleum volatile organic compounds (VOCs) condensation recovery system combined with mixed-refrigerant refrigeration. International Journal of Refrigeration, 116, 23-35. https://doi.org/10.1016/j.ijrefrig.2020.03.011
[9] Pontes-López, S., Moreno, J., Esteve-Turrillas, F.A., Armenta, S., 2020. Development of a simulation chamber for the evaluation of dermal absorption of volatile organic compounds. Atmospheric Pollution Research, 11(5), 1009-1017. https://doi.org/10.1016/j.apr.2020.02.015
[10] Qi, D., Liu, Y., Liu, Y., Liu, Z., Luo, Y., Xu, H., Zhou, X., Zhang, J., Yang, H., Wang, W., Chen, X., 2020. Polymeric Membranes with Selective Solution-Diffusion for Intercepting Volatile Organic Compounds during Solar-Driven Water Remediation. Advanced Materials, 32(50), 2004401. https://doi.org/10.1002/adma.202004401
[11] Wu, M., Huang, H., Leung, D.Y., 2022. A review of volatile organic compounds (VOCs) degradation by vacuum ultraviolet (VUV) catalytic oxidation. Journal of Environmental Management, 307, 114559. https://doi.org/10.1016/j.jenvman.2022.114559
[12] Assadi, H., Armaghan, F., Taheri, R.A., 2021. Photocatalytic oxidation of ketone group volatile organic compounds in an intensified fluidized bed reactor using nano-TiO2/UV process: an experimental and modeling study. Chemical Engineering and Processing-Process Intensification, 161, 108312. https://doi.org/10.1016/j.cep.2021.108312

[13] Hossain, M.M., Mok, Y.S., Nguyen, V.T., Sosiawati, T., Lee, B., Kim, Y.J., Lee, J.H., Heo, I., 2022. Plasma-catalytic oxidation of volatile organic compounds with honeycomb catalyst for industrial application. Chemical Engineering Research and Design, 177, 406-417. https://doi.org/10.1016/j.cherd.2021.11.010
[14] Mokhtari, M., Hajizadeh, Y., Ebrahimi, A.A., Shahi, M.A., Jafari, N., Abdolahnejad, A., 2019. Enhanced biodegradation of n-hexane from the air stream using rhamnolipid in a biofilter packed with a mixture of compost, scoria, sugar beet pulp and poplar tree skin. Atmospheric Pollution Research, 10(1), 115-122. https://doi.org/10.1016/j.apr.2018.06.008
[15] Golmohammadi, M., Hassankiadeh, M.N., Zhang, L., 2021. Facile biosynthesis of SnO_2/ZnO nanocomposite using Acroptilon repens flower extract and evaluation of their photocatalytic activity. Ceramics International, 47(20), 29303-29308. https://doi.org/10.1016/j.ceramint.2021.07.095
[16] Golmohammadi, M., Honarmand, M., Esmaeili, A., 2022. Biosynthesis of ZnO nanoparticles supported on bentonite and the evaluation of its photocatalytic activity. Materials Research Bulletin, 149, 111714. https://doi.org/10.1016/j.materresbull.2021.111714
[17] Debono, O., Hequet, V., Le Coq, L., Locoge, N., Thevenet, F., 2017. VOC ternary mixture effect on ppb level photocatalytic oxidation: Removal kinetic, reaction intermediates and mineralization. Applied Catalysis B: Environmental, 218, 359-369. https://doi.org/10.1016/j.apcatb.2017.06.070
[18] Wei, Z.S., He, Y.M., Huang, Z.S., Xiao, X.L., Li, B.L., Ming, S., Cheng, X.L., 2019. Photocatalytic membrane combined with biodegradation for toluene oxidation. Ecotoxicology and environmental safety, 184, 109618. https://doi.org/10.1016/j.ecoenv.2019.109618
[19] Kundu, S., Karak, N., 2022. Polymeric photocatalytic membrane: An emerging solution for environmental remediation. Chemical Engineering Journal, 135575. https://doi.org/10.1016/j.cej.2022.135575
[20] Nasrollahi, N., Ghalamchi, L., Vatanpour, V., Khataee, A., 2021. Photocatalytic-membrane technology: a critical review for membrane fouling mitigation. Journal of Industrial and Engineering Chemistry, 93, 101-116. https://doi.org/10.1016/j.jiec.2020.09.031
[21] Li, J., Li, B., Sui, G., Du, L., Zhuang, Y., Zhang, Y., Zou, Y., 2021. Removal of volatile organic compounds from air using supported ionic liquid membrane containing ultraviolet-visible light-driven Nd-TiO_2 nanoparticles. Journal of Molecular Structure, 1231, 130023. https://doi.org/10.1016/j.molstruc.2021.130023
[22] Matsumoto, M., Inomoto, Y., Kondo, K., 2005. Selective separation of aromatic hydrocarbons through supported liquid membranes based on ionic liquids. Journal of Membrane Science, 246(1), 77-81. https://doi.org/10.1016/j.memsci.2004.08.013
[23] Yan, X., Anguille, S., Bendahan, M., Moulin, P., 2019. Ionic liquids combined with membrane separation processes: A review. Separation and Purification Technology, 222, 230-253. https://doi.org/10.1016/j.seppur.2019.03.103
[24] Solangi, N.H., Anjum, A., Tanjung, F.A., Mazari, S.A., Mubarak, N.M., 2021. A review of recent trends and emerging perspectives of ionic liquid membranes for CO_2 separation. Journal of Environmental Chemical Engineering, 9(5), 105860. https://doi.org/10.1016/j.jece.2021.105860
[25] Malayeri, M., Haghighat, F., Lee, C.-S., 2019. Modeling of volatile organic compounds degradation by photocatalytic oxidation reactor in indoor air: A review. Building and Environment, 154, 309-323. https://doi.org/10.1016/j.buildenv.2019.02.023
[26] Ranade, V.V., 2002. Computational flow modeling for chemical reactor engineering, Academic press.
[27] Sitaru, G., Gekle, S., 2022. Analytical and computational study of cascade reaction processes in catalytic fibrous membranes. Computers & Fluids, 240, 105438. https://doi.org/10.1016/j.compfluid.2022.105438
[28] Phan, D.D., Babick, F., Nguyen, M.T., Wessely, B., Stintz, M., 2017. Modelling the influence of mass transfer on fixed-bed photocatalytic membrane reactors. Chemical Engineering Science, 173, 242-252. https://doi.org/10.1016/j.ces.2017.07.043
[29] Zak, N., Marks, R., Perez-Calleja, P., Nerenberg, R., Doudrick, K., 2020. A computational model for the catalytic hydrogel membrane reactor. Water Research, 185, 116199. https://doi.org/10.1016/j.watres.2020.116199
[30] Multiphysics, C., 2019. v. 5.2, COMSOL AB, Stockholm, Sweden. Google Scholar.
[31] Lee, S., Park, G., Amy, G., Hong, S.-K., Moon, S.-H., Lee, D.-H., et al., 2002. Determination of membrane pore size distribution using the fractional rejection of nonionic and charged macromolecules. Journal of Membrane Science, 201(1-2), 191-201. https://doi.org/10.1016/S0376-7388(01)00729-3
[32] Green, D.W., Southard, M.Z., 2019. Perry's chemical engineers' handbook, McGraw-Hill Education.